Journal Pre-proof

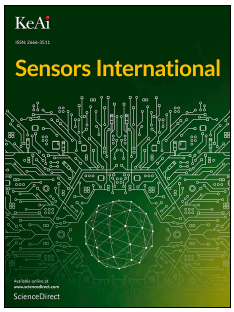

Commercial Chip-based Tunneling Magnetoresistance Sensor for Green-synthesized Magnetic Nanoparticles Assay

Pinaka Elda Swastika, Harlina Ardiyanti, Zurnansyah, Deska Lismawenning Puspitarum, Nurul Imani Istiqomah, Nur Aji Wibowo, Edi Suharyadi

PII: S2666-3511(24)00010-X

DOI: https://doi.org/10.1016/j.sintl.2024.100288

Reference: SINTL 100288

To appear in: *Sensors International*

Received Date: 19 March 2024

Revised Date: 24 June 2024

Accepted Date: 28 July 2024

Please cite this article as: P.E. Swastika, H. Ardiyanti, Zurnansyah, D.L. Puspitarum, N.I. Istiqomah, N.A. Wibowo, E. Suharyadi, Commercial Chip-based Tunneling Magnetoresistance Sensor for Green-synthesized Magnetic Nanoparticles Assay, *Sensors International*, https://doi.org/10.1016/j.sintl.2024.100288.

Commercial Chip-based Tunneling Magnetoresistance Sensor for Green-synthesized Magnetic Nanoparticles Assay

Pinaka Elda Swastika[1,2], Harlina Ardiyanti[1,3], Zurnansyah[1], Deska Lismawenning Puspitarum[1,3], Nurul Imani Istiqomah[1], Nur Aji Wibowo[4], Edi Suharyadi[1]*

[1]Department of Physics, Universitas Gadjah Mada, Yogyakarta, Indonesia
[2]Department of Physics Education, Universitas Negeri Yogyakarta, Yogyakarta, Indonesia
[3]Department of Physics, Institut Teknologi Sumatera, Lampung, Indonesia
[4]Department of Physics, Universitas Kristen Satya Wacana, Salatiga, Indonesia

*****Corresponding author: esuharyadi@ugm.ac.id

Abstract

Owing to their significant roles in multiple sectors, the demand for high-performance, rapid, user-friendly, and low-cost sensors is crucial for biosensing. This paper reports the performance of a commercial chip-based tunneling magnetoresistance (TMR) sensor for detecting green-synthesized magnetic nanoparticles (MNP) as potential magnetic labels. A Simple and low-cost design consisting of a TMR chip ALT-025 integrated with an Arduino microcontroller and a basic differential amplifier was developed to provide real-time and measurable digital readouts. Three kinds of ferrite MNPs (Fe_3O_4, $CoFe_2O_4$ and $MnFe_2O_4$) was synthesized by the coprecipitation method on the green synthesis approach utilizing *Moringa Oleifera* extracts. All sample have a face-centered cubic inverse spinel structure with average grain size of 10.3 nm, 9.2 nm and 6.1 nm for Fe_3O_4, $CoFe_2O_4$ and $MnFe_2O_4$, respectively. Furthermore, soft ferromagnetic behavior is identified for all sample with magnetization saturation of 55.3 emu/g, 37.6 emu/g, 19.3 emu/g for Fe_3O_4, $CoFe_2O_4$ and $MnFe_2O_4$, respectively. The sensor showed a promising performance in the detection of MNPs. For the three particles, the sensitivity exhibited a linear function of the MNPs concentration. The sensitivity is related not only to the particle size but also to the magnetization of the nanoparticles in the bias field. The change in the output voltage was proportional to the bias magnetization (M_{Bias}), indicating that particles with a higher bias magnetization can produce a stronger magnetic stray field on the TMR sensor surface. The sensor system successfully detected MNPs at different stray field intensities. Furthermore, a low limit of detection was achieved using these methods. Moreover, the remarkable stability and repeatability of the sensor is further validated by the steady signal acquired for 30s with an RSD of 0.5-28.5%. Therefore, the integration of commercial chip-based TMR sensors and green-synthesized MNPs has great potential for advancing the detection of various biomolecules.

Keywords: sensor, tunneling magnetoresistance, commercial chip, green synthesis, ferrite nanoparticles

1. Introduction

Biosensing now plays a significant role in several domains, such as healthcare, food safety, and environmental and industrial monitoring[1–7]. Therefore, it is important to develop a sensor that uses high-performance, rapid, user-friendly, low-cost, compact, and compatible semiconductor fabrication technologies. Currently, the prevalent type of biosensor detection involves the use of labels, such as fluorescent materials, colloidal gold, quantum dots, and up-conversion luminous materials. This type of biosensor detects color changes induced by target

molecules. Overcoming color interference in complex environmental samples is challenging[3,8]. Magnetic sensors coupled with magnetic nanoparticles (MNPs) are a compelling alternative for biomolecular detection. Unlike typical labeled biosensors based on optical signal detection, magnetic signal detection is unaffected by background color or optical signals created by field-complex environmental samples[3,9]. Furthermore, the properties of MNPs as labels can be easily tailored during synthesis for specific applications[10,11].

Magnetic field sensing methods include magnetoimpedance (MI) and magnetoresistance (MR) sensors such as giant magnetoimpedance (GMI), anisotropic magnetoresistance (AMR), giant magnetoresistance (GMR), and tunneling magnetoresistance (TMR). These sensors operate on the basis of the MI or MR effect, wherein the impedance or resistance of the sensing material changes in response to an external magnetic field[12]. AMR and GMI sensors are known to exhibit reduced levels of comparable magnetic noise. Nevertheless, in the context of AMR, magnetization exhibits two potential orientations upon exposure to strong magnetic fields, resulting in an unstable output from the sensor[13]. However, in GMI, intricate design and manufacturing processes impede practical implementation and large-scale production. [14]. Among the MR-based sensors, GMR sensors have attracted the attention of researchers. This is because the functional area of a GMR sensor is vast. Furthermore, thin metal films, which are the building blocks of GMR sensors, can be deposited easily[8]. Nevertheless, TMR exhibits a higher MR ratio with greater stability and better sensitivity for detecting small changes in magnetic fields[9,15,16]. Moreover, the TMR sensor requires only a small sample size during testing, which makes it convenient and cost-effective[3].

The operation of the TMR sensor is based on the spin-dependent tunneling effect. In the MNPs assay, the TMR sensor detects the stray fields of MNPs generated by an external magnetic field. The change in the stray-field intensity affects the differential magnetization of the adjacent ferromagnetic layers. Consequently, the probability of electron tunneling is altered, leading to a change in the resistance[17]. Therefore, MNPs play a crucial role in TMR sensor detection systems because they have the potential to influence the output signal and sensitivity of the sensor.

Researchers have made concerted efforts to enhance the detection performance by selecting distinct magnetic particles as labels. Owing to their inherent advantages, including controllable size, physical and chemical characteristics, and low production costs, ferrite-based MNPs have emerged as a prominent option among the various magnetic nanomaterials that have been explored for biosensing applications[18]. The properties of ferrite-based MNPs vary widely in size, structure, composition, and morphology; therefore, they can be easily controlled during synthesis[19]. At sizes less than 20 nm, ferrite-based MNPs exhibit high saturation magnetization (M_s) and near-zero remnant magnetization (M_r), making them very responsive to external magnetic fields[20]. Multiple studies have been conducted on the detection of ferrite-based MNPs using MR-based sensors. However, most of the sensors used are GMR sensors. Jin et al. used a TMR thin film to detect Fe_3O_4 [15], and Xu et al. used a GMR chip sensor to detect $MnFe_2O_4$ [21]. Zhang et al. then utilized the same GMR sensor to detect four distinct types of ferrite particles ($CoFe_2O_4$, $NiFe_2O_4$, $NiZnFe_2O_4$ dan γ-Fe_2O_3) to examine how the magnetic properties of the label particles affected the signal and sensitivity of the sensor[22]. In addition, Zhang et al. reported that the GMR sensor performance was affected by the size of Fe_3O_4[23]. Our previous study also reported the development of a GMR sensor to detect Fe_3O_4 MNPs with thin-film multilayer Co/Cu and spin-valve CoFeB as sensing elements[24–28]. In all these studies, owing to the low output voltage, a costly instrument such as a voltmeter is still required.

Most research has employed MNPs produced through chemical synthesis methods that require time-consuming and energy-consuming processes, costly ingredients, and hazardous byproducts. Therefore, an alternative green synthesis approach is proposed that uses plant

extracts or microorganisms [29,30] that are considered superior in terms of biocompatibility, environmental friendliness, nontoxicity, and waste reduction during the production process[31,32]. Green synthesis of MNPs using plant extracts has been accomplished in several experiments, and the MNPs still exhibit good magnetic properties[33–40]. *Moringa Oleifera* (MO) is often used as a primary ingredient for the green synthesis of nanoparticles owing to the abundant presence of phytochemical compounds, including phenolics and flavonoids. These chemicals serve as both reducing agents and stabilizers during synthesis [41–44]. Our previous research successfully produced green-synthesized Fe_3O_4 using MO extract. This Fe_3O_4 employed as an MNPs label in the GMR biosensor. These findings demonstrate that the green-synthesized Fe_3O_4 has promising characteristics as a label in a small bias field[45–47].

Recently, several nanotechnology companies have successfully manufactured sensors in the form of chips. The miniaturization of sensors will considerably boost portable lab-on-chip development for rapid on-site detection[9]. Nonvolatile Electronics (NVE) Corp. manufactures the TMR sensor chips and releases them commercially. The TMR sensors produced by the NVE were labeled ALT-025 and comprised active TMR sensors arranged in a Wheatstone bridge configuration. This configuration can prevent temperature drift and increase the sensor stability and sensitivity. Moreover, it can reduce the hysteresis effects and increase the linearity of the sensor output[48,49]. The ALT-025 sensors offer a wide range of linearity (0.001–10 mT), compact dimensions (2.5 × 2.5 mm), and are available at an affordable price ($5.68–$12.00)[50]. Because of the presence of two analog outputs in the Wheatstone bridge configuration, sensor sensitivity can be instantly enhanced using a basic differential operational amplifier (OA). Furthermore, this amplified signal can be conveniently linked to a microcontroller such as an Arduino. Arduino is a widely used microcontroller owing to its open-source software, comprehensive libraries, low cost, user-friendly interface, and ease of development[51]. It converts the analog output of the sensor into a digital format that is promptly recorded and stored as a text file. In previous studies, Wibowo et al. and Ardiyanti et al.. proposed a new platform-based GMR chip sensor equipped with a basic amplifier circuit and Arduino microcontroller to detect iron-based MNPs[46,52]. The integration of a microcontroller system with a chip sensor resulted in the development of a simple, cost-effective, and rapid sensor for MNPs.

Despite their high sensitivity, research related to the coupling of TMR sensors and MNPs is limited. Furthermore, we have not found any reports on green-synthesized magnetic label detection using TMR sensors. The exploration of green-synthesized MNPs as labels for TMR-based sensors remains challenging. Therefore, to the best of our knowledge, this study aims to develop a simple and low-cost commercial chip-based TMR sensor coupled with green-synthesized MNPs as potential magnetic labels. The ALT-025 TMR chip, which served as the sensing material in our system, was integrated with a basic differential OA and Arduino microcontroller to produce a measurable output voltage and real-time digital readout. The performance of the TMR sensor was evaluated by detecting three types of ferrite-based MNPs (Fe_3O_4, $CoFe_2O_4$, $MnFe_2O_4$) that represent varying particle sizes and magnetic properties. Therefore, it is vital to determine an appropriate value. Exploring appropriate magnetic labels and their influence on the detection signals may pave the way for the development of more advanced magnetic biosensors.

2. Experimental Methods

2.1 Green Synthesis of Magnetic Nanoparticles

Preparation of MO Extract: Water-based extraction was performed at a 1:12 (w/v) ratio. The MO leaf extract powder was diluted in deionized (DI) water and heated at 60 °C under

stirring for 1 h. Then, the mixture was filtered using Whatman 01 paper after cooling to room temperature. The resulting MO extract was stored in a refrigerator until use in the subsequent synthesis.

Green Synthesis of Fe_3O_4: Green-synthesized MNP labels were obtained by co-precipitation method, as previously reported. For Fe_3O_4, $FeSO_4 \cdot 7H_2O$ and $FeCl_3 \cdot 6H_2O$ were used as Fe^{3+} and Fe^{2+} ion sources, respectively. A mixture of these precursors at a 1:2 molar ratio was dissolved in DI water and stirred for 15 min. Next, MO extract was added while stirring at 60 °C, then followed by the dropwise addition of a 10% ammonia solution for 90 min. The color of the mixture changed from greenish-black to black, indicating the formation of Fe_3O_4. After cooling to ambient temperature, the precipitate was separated from the solution by magnetic decantation and rinsed with DI water until the pH reached 7. Finally, the precipitated Fe_3O_4 was dried at 100 °C for 2 h.

Green Synthesis of $CoFe_2O_4$: The first step to obtain $CoFe_2O_4$ was to mix $CoCl_2 \cdot 6H_2O$ and $FeCl_3 \cdot 6H_2O$ (1:2 molar ratio) in DI water. These materials were the sources of Co and Fe ions, respectively. Subsequently, the MO extract was added, and the mixture was stirred for 30 min at room temperature. The resulting solution is denoted as Solution A. Meanwhile, 1.5 M NaOH was diluted in 25 ml DI water and stirred for 15 min at 80 °C. Subsequently, Solution A was added dropwise to the NaOH solution at 80 °C for 60 min. After the brownish-black precipitate reached room temperature, it was removed from the solution using an external magnet and washed several times with DI water. Then, the precipitate was dried at 80 °C for 7 h. Finally, the dried precipitate was calcinated for 5.5 h at 600 °C, resulting black $CoFe_2O_4$ powder.

Green Synthesis of $MnFe_2O_4$: Synthesis of $MnFe_2O_4$ is similar to that of $CoFe_2O_4$. The distinction is that it employs $MnCl_2 \cdot 6H_2O$ as a source of Mn ions, whereas NaOH has a molarity of 5. $MnFe_2O_4$ was calcined at the same temperature and time.

2.2 Material Characterization

The crystal structure and phase of the MNPs were identified by X-Ray diffraction (XRD) using Shimadzu XD-3H with Cu-kα radiation. Transmission electron microscopy (TEM, JEOL JEM-1400) was used to observe morphology and size distribution. Scanning electron microscopy (SEM) with energy-dispersive X-ray spectroscopy (EDX) was used to examine the surface morphology and elemental mapping of the nanoparticles. The magnetic properties of the MNPs were measured using a vibrating-sample magnetometer (VSM, Riken Denshi Co., Ltd.).

2.3 TMR Sensor Detection System

In this study, a Wheatstone Bridge TMR sensor chip ALT-025 was used as the sensing material. Figure 1 (a) shows an image of ALT-025 and its layout. Figure 1(b) shows a schematic of the experimental setup. The DC power supply was coupled to a Helmholtz coil to provide an in-plane magnetic field (H) along the easy axis of the sensor. To study the effect of the magnetic properties on the detection signals, three types of green-synthesized ferrite samples were prepared by dispersing them in ethanol at different concentrations (2.0, 4.0, 10, 20, 25, and 30 mg/mL). MNPs-ethanol dispersion (2 μL) was applied to the TMR chip surface by drop casting. After 15 min, the ethanol was evaporated, and the bias magnetic field (H_{Bias}) generated by the Helmholtz coil was triggered along the easy axis of the TMR chip. The output voltage was measured consecutively for 30 s.

Figure 1(c) shows a circuit diagram of the data acquisition system. The analog output of the TMR chip was amplified using an OA LM358 IC and a basic differential amplifier. This IC has a high voltage gain of up to 100 dB, allowing for a flexible output-voltage amplification

circuit design. A differential amplifier magnifies the difference between the two input voltages by suppressing the simultaneous voltages on both inputs[52]. This circuit offers benefits, such as noise suppression and reduced external interference. The use of large resistor in this work (6.7 MΩ for R_{ref} and 100 kΩ for R_{in}) aims to reduce the resistance inside the internal circuit. A single amplified analog output from the OA was converted into a digital output using an Arduino UNO ATMEGA 328 microcontroller (10 bit). The signal was then collected and analyzed using a computer for rapid data collection. An Arduino microcontroller was also utilized to power the TMR chip sensor and LM358 via pins of 5V and GND. The inclusion of ADS1115 (16 bits) is intended to boost the data resolution. The microcontroller generated a single digital voltage that was smoothed using a Savitzky–Golay (SG) filter. The sensor system is well suited for an SG filter because of its comparatively high signal-to-noise ratio (SNR), which ensures preservation of the initial signal value[53]. To compensate for environmental disturbances like background voltage and geomagnetic field, the sensor signal is calculated by subtracting the smoothed output voltage with the MNPs (V_O) from the smoothed output voltage of the bare-chip (sensor without MNPs) ($V_{O\text{-chip}}$), as expressed in Eq. (1).

$$\text{Signal} = \left|V_O\text{-}V_{O\text{-chip}}\right| \qquad \text{(Eq.1)}$$

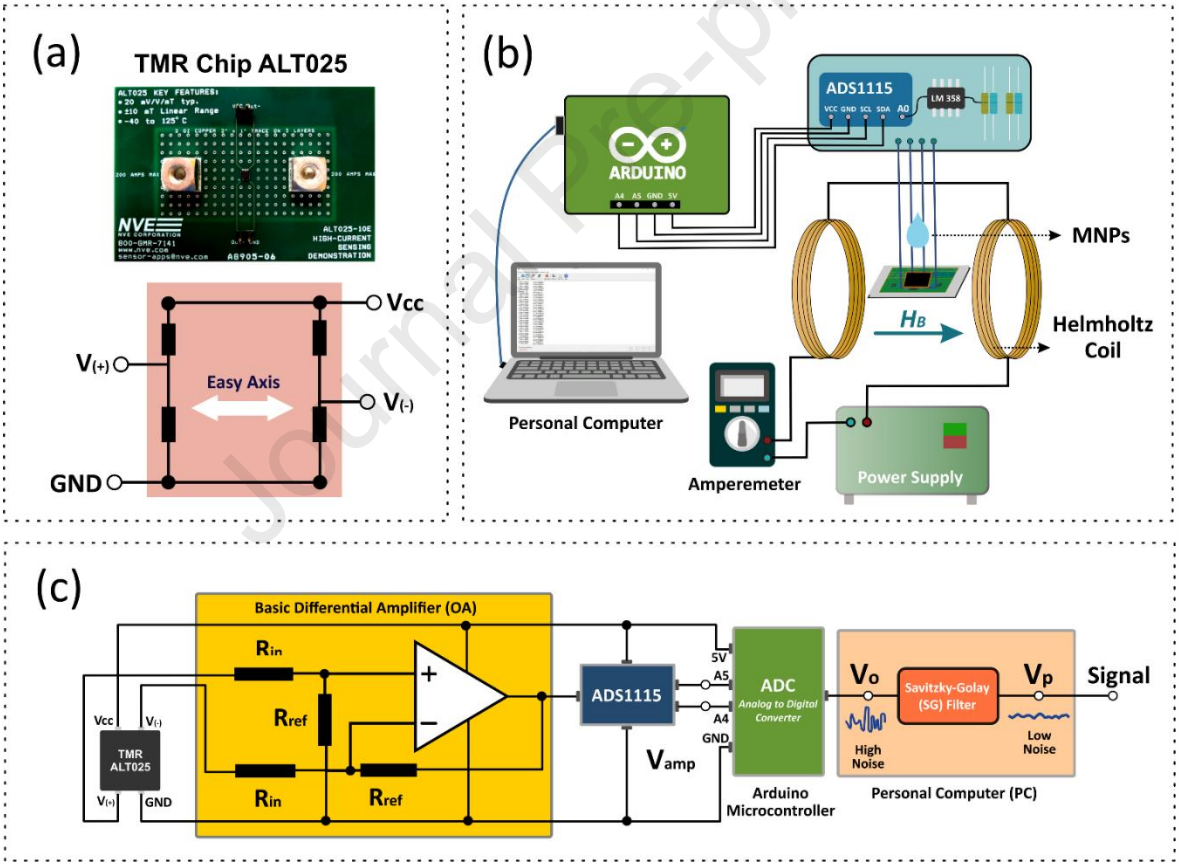

Fig. 1. (a) Photograph and layout of NVE TMR chip, (b) schematic of experimental setup, and (c) circuit diagram of the data acquisition system.

3. Results and Discussion

3.1 Characteristics of MNPs Label

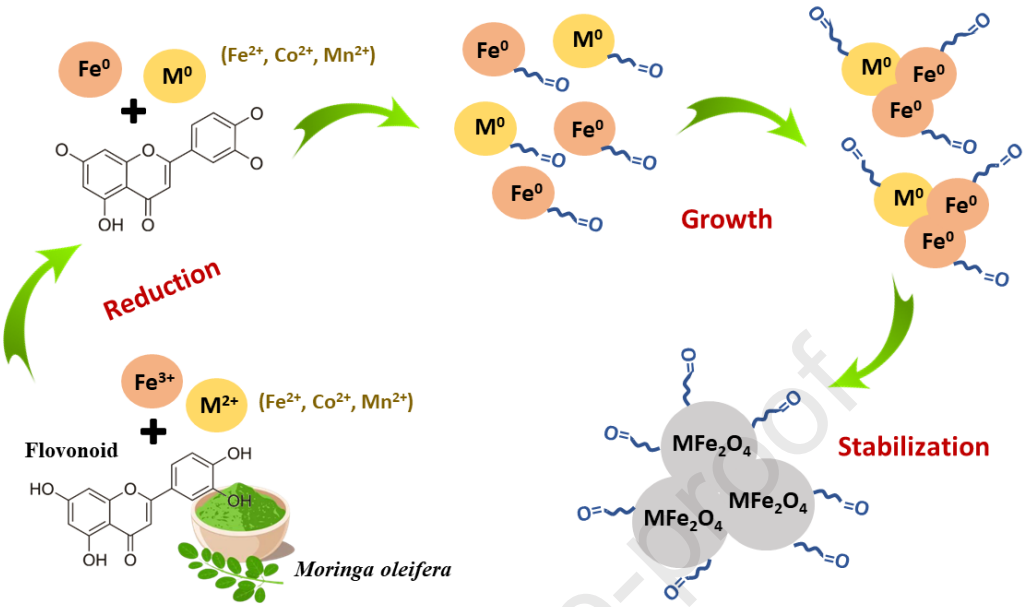

Fig. 2. Mechanism of green-synthesized MNPs

In this study, a green synthesis method was devised to produce MO-based MNPs, such as Fe_3O_4, $CoFe_2O_4$ and $MnFe_2O_4$. In general, nanoparticles can be separated into three distinct phases, as shown in Fig. 2. The first is the reduction. Throughout this stage, the metal ions are reduced as a result of the hydroxyl groups (–OH) in the flavonoids present in the MO extract reacting with them and transforming the flavonoids from their enol to keto forms. Subsequently, nucleation occurred. During the growth phase, the nanoparticles coalesce and grow to specific sizes and morphologies. In the last phase, known as stabilization, the formation activity reaches its peak when the nanoparticles reach a stable size and shape[54,55].

3.1.1 XRD Analysis

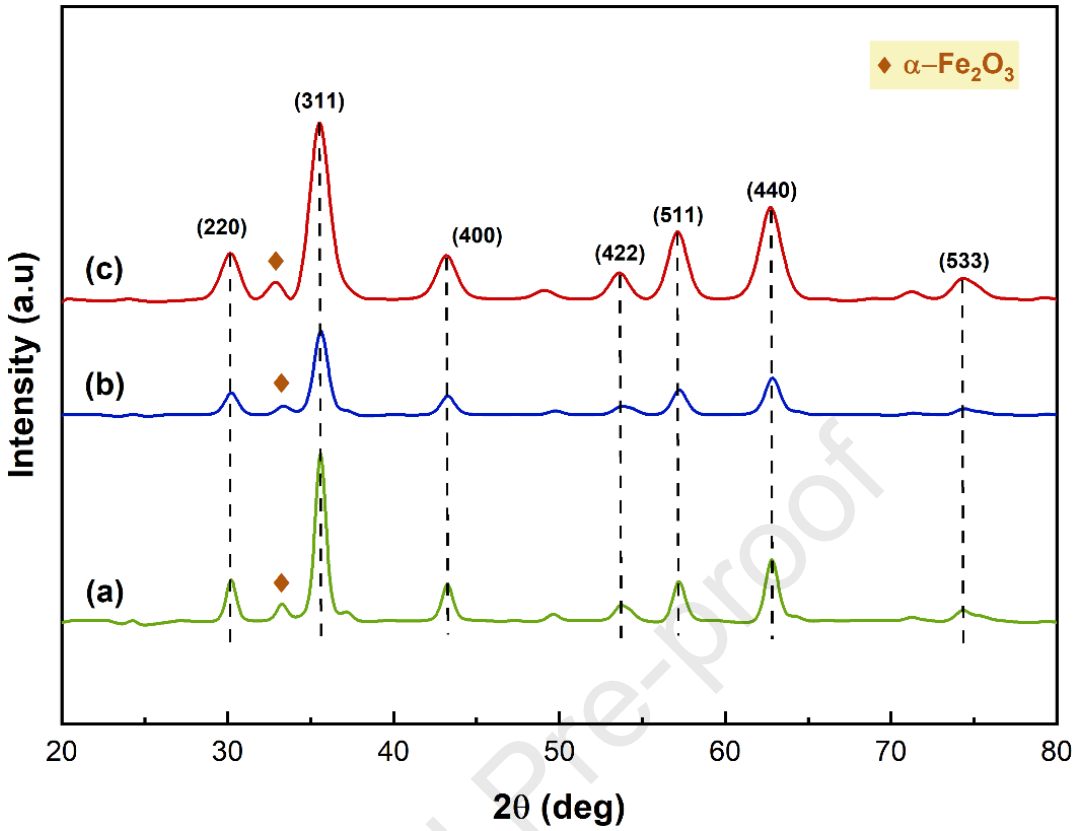

Fig. 3. XRD patterns of (a) Fe_3O_4, (b) $CoFe_2O_4$, and (c) $MnFe_2O_4$.

Figure 3 shows the XRD patterns of Fe_3O_4, $CoFe_2O_4$ and $MnFe_2O_4$ analyzed by Rietveld refinement using MAUD. The three types of as-synthesized MNPs exhibited a face-centered cubic inverse spinel structure (Fd-3m space group), which was confirmed by the presence of diffraction peaks corresponding to the (220), (311), (400), (422), (511), (440), and (533) planes. These peaks match well with the standard powder diffraction data for Fe_3O_4 (COD-1010369), $CoFe_2O_4$ (COD-1533163), and $MnFe_2O_4$ (COD-2300585). In the interim, the appearance of a peak at $2\theta = \sim 33^o$ shows that another phase has developed as a minor impurity. This occurs when samples are likely exposed to oxygen during the drying and preparation process, causing them to undergo a phase transition to hematite (α-Fe_2O_3) as a results of oxidation reaction[56].

Table 1 lists the calculated crystallite sizes and lattice parameters for all samples. These results represent the mean values calculated for all peaks that correspond to the standard data. From the peak widths, the average crystalline size is estimated to be 9.3 nm, 7.6 nm, and 6.0 nm for Fe_3O_4, $CoFe_2O_4$ and $MnFe_2O_4$, respectively. The Debye-Scherrer equation was used to calculate the values. Bragg's law was used to estimate the lattice parameters of the ferrite nanoparticles. The lattice parameters of Fe_3O_4, $CoFe_2O_4$ and $MnFe_2O_4$ are 8.36, 8.35, and 8.37, respectively. These values are consistent with findings from other reports on the green synthesis of MNPs, as shown in Table1.

Table 1. Crystallite size and lattice parameter of Fe_3O_4, $CoFe_2O_4$, and $MnFe_2O_4$.

Sample	Crystallite Size (nm)	Lattice Parameter (Å)	Lattice Parameter Reported by Other (Å)
Fe_3O_4	9.7 ± 0.2	8.36 ± 0.06	8.35 - 8.38 [57,58]
$CoFe_2O_4$	7.9 ± 0.2	8.35 ± 0.07	8.32 - 8.39 [29,33,59]
$MnFe_2O_4$	6.0 ± 0.2	8.37 ± 0.01	8.34 - 8.59 [60–62]

3.1.2 TEM Analysis

The morphology and size distribution of the MNPs were examined by TEM. Fe_3O_4, $CoFe_2O_4$ and $MnFe_2O_4$ are nearly spherical. The images in Fig. 4 clearly show that Fe_3O_4 and $CoFe_2O_4$ exhibited better dispersion, whereas $MnFe_2O_4$ tended to agglomerate, resulting in the formation of larger particles. The observed agglomeration is likely due to the high surface-area-to-volume ratio, magnetic attraction, strong van der Waals forces, and interactions within the particles[55]. The average grain size of Fe_3O_4, $CoFe_2O_4$ and $MnFe_2O_4$ are 10.3 ± 2.2 nm, 9.2 ± 1.7 nm, and 6.1 ± 1.5 nm, respectively. Using a normal distribution function, these values were estimated statistically for over 100 randomly selected MNPs from the TEM images. These findings are close to the crystallite size values obtained from the XRD analysis.

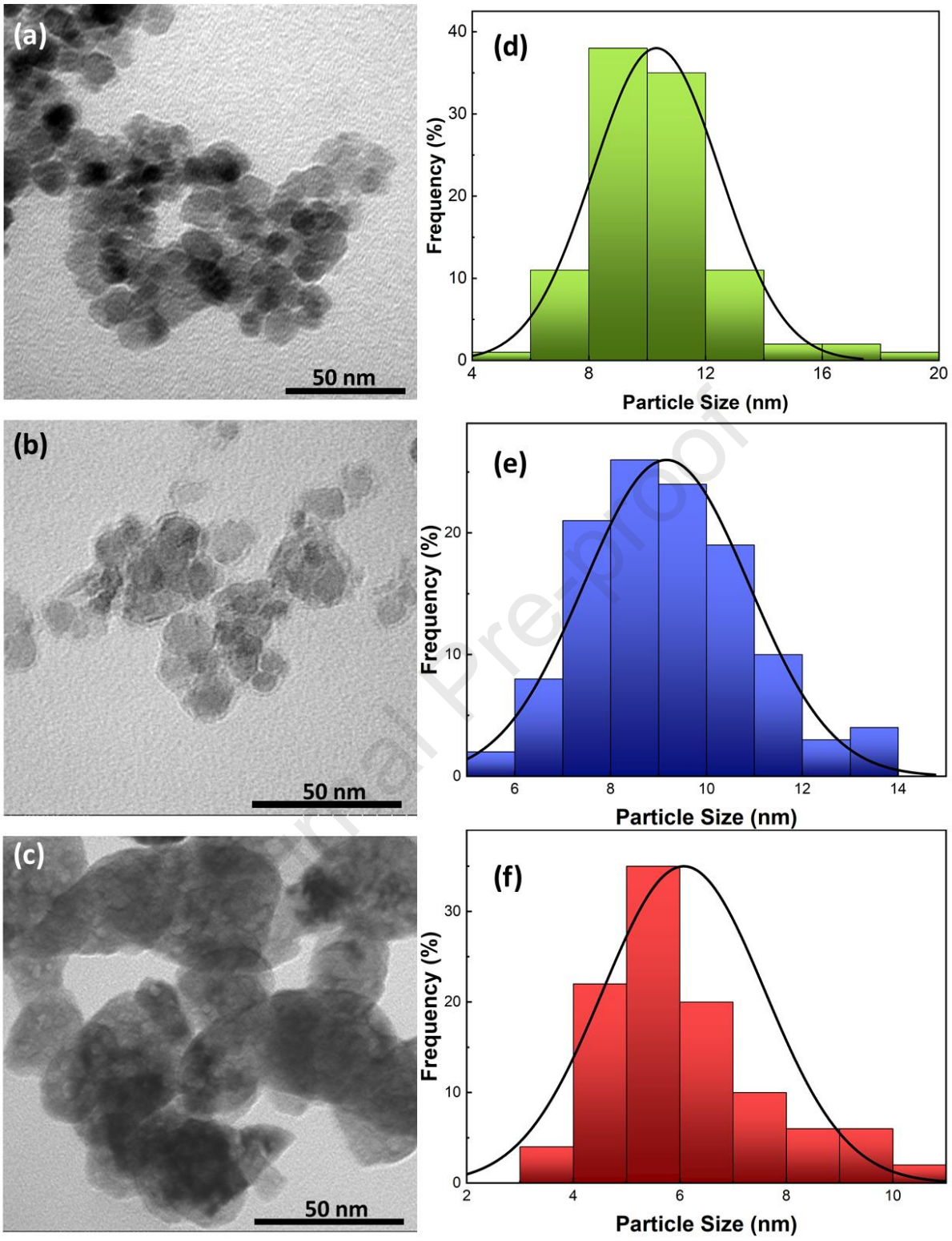

Fig. 4. TEM images of (a) Fe_3O_4, (b) $CoFe_2O_4$, (c) $MnFe_2O_4$ and particle size distributions of (d) Fe_3O_4, (e) $CoFe_2O_4$, (f) $MnFe_2O_4$.

3.1.3 SEM-EDX Analysis

The surface topography and elemental mapping of the MNPs were examined using SEM-EDX. Figure 5 reveals that all the samples exhibited inhomogeneous shapes and considerable aggregation. Elemental mapping revealed a uniform distribution of the constituent elements of each ferrite on the sample surface, with no impurities detected. This indicated that Fe_3O_4, $CoFe_2O_4$ and $MnFe_2O_4$ were successfully formed. The EDX results for Fe_3O_4 show that the weight percentages of Fe and O are 70.87% and 29.13%, respectively. In contrast, for $CoFe_2O_4$, the weight percentages of Co, Fe, and O are 24.13%, 31.83%, and 44.04%, respectively. Finally, the weight percentages of Mn, Fe, and O in the $MnFe_2O_4$ sample were 18.90%, 39.46% and 41.64%, respectively.

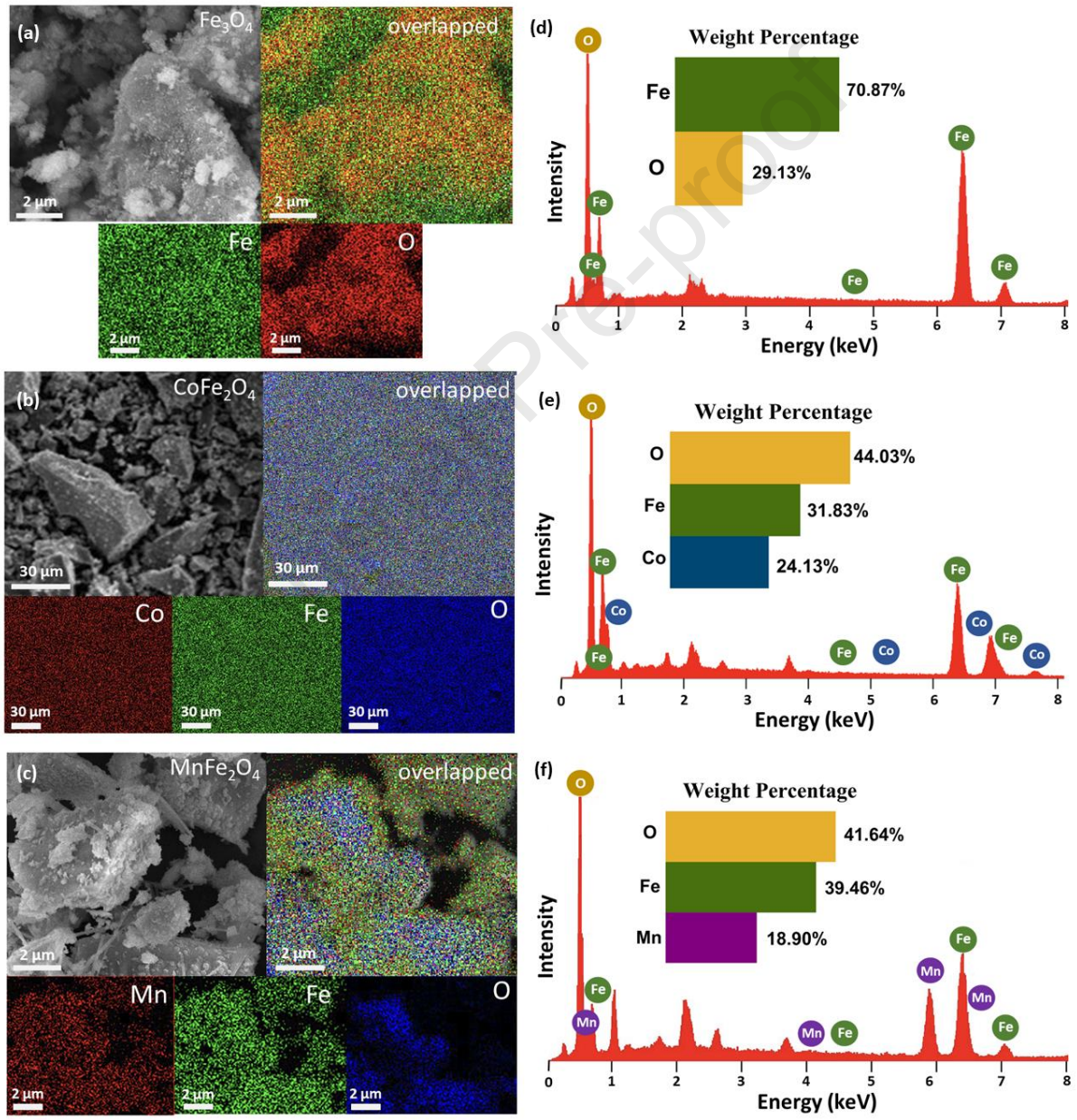

Fig. 5. SEM images and mapping analysis of (a) Fe_3O_4, (b) $CoFe_2O_4$, (c) $MnFe_2O_4$ and EDX spectrum of (d) Fe_3O_4, (e) $CoFe_2O_4$, (f) $MnFe_2O_4$.

3.1.4 Magnetic Properties Analysis

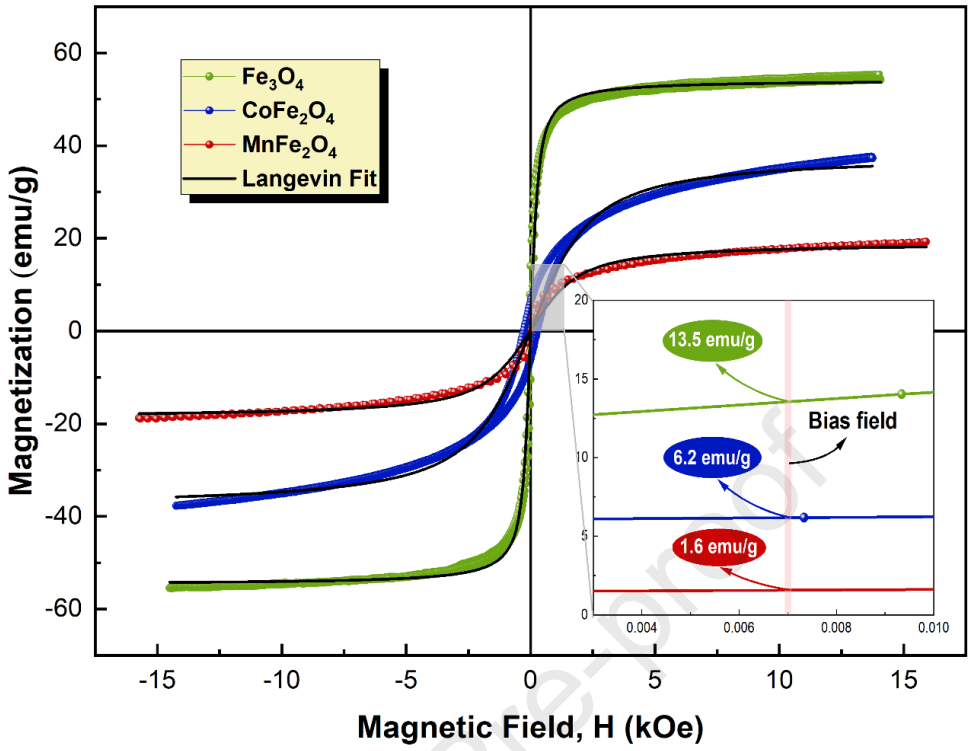

Fig. 6. The magnetic hysteresis loop curves of Fe_3O_4, $CoFe_2O_4$, $MnFe_2O_4$ and magnetization at 7 Oe.

The magnetic properties of the as-synthesized MNPs were evaluated using VSM, and are depicted as hysteresis loops in Fig. 6. These properties are important features of TMR-based sensors. All samples exhibited soft ferromagnetic behavior, as evidenced by their low remanence (M_r) and coercivity (H_c). The presence of α-Fe_2O_3 in the sample is responsible for the non-zero coercivity field. Consequently, the exchange bias may have resulted from the antiferromagnetic nature of the hematite[45]. The magnetization saturation (M_s) of Fe_3O_4, $CoFe_2O_4$, and $MnFe_2O_4$ are approximately 54.4 emu/g, 38.3 emu/g and 18.9 emu/g, respectively, showing an increase with particle size. As the particle size increases, M_s increases owing to a reduction in defects, deformations, and disorders[63]. When the NPs become larger, the surface spin-disorder effect decreases because of the decrease in the surface-to-volume ratio, and the Ms value can increase, approaching that of the bulk[64]. The inset image shows the magnetization of samples at the bias field (H_{Bias} = 7 Oe), with values are approximately 13.5 emu/g, 6.2 emu/g and 1.6 emu/g for Fe_3O_4, $CoFe_2O_4$, and $MnFe_2O_4$, respectively. There is a positive correlation between the nanoparticle size and both the saturation magnetization and magnetization during the bias field (M_{Bias})[23]. The discussion in the ensuing section provides further details on how the discrepancy in magnetic performance under a bias field significantly affects detection outcomes.

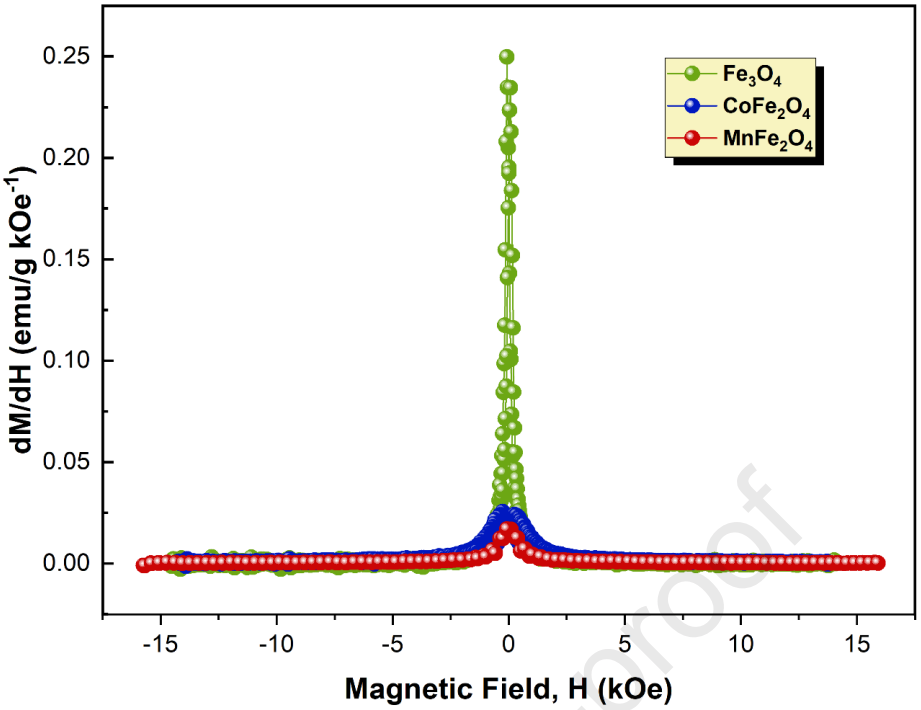

Fig. 7. The switching field distribution at room temperature of dM/dH versus H for MNPs

Subsequently, a fitting analysis was performed using the Langevin function to ascertain other magnetic property characteristics, such as magnetic susceptibility (χ) and domain size (D_m). Table 2 displays the calculated results for these properties. χ refers to capability of magnetic material to be magnetized when exposed to an external magnetic field [65]. Based on the obtained data in Table 2, reducing the value of M_s will lead to a proportional decrease in χ. This implies that a higher value of M_s corresponds to a stronger reaction to the external magnetic field. Figure 7 illustrates the switching field distribution at room temperature for MNPs. dM/dH at H=0 is initial magnetic susceptibility (χ_i). All nanomaterials have Xi values at zero magnetic field, indicating that the materials can be easily magnetized owing to the impact of thermal energy and very small particle size[66]. The anisotropy constant for Fe_3O_4, $CoFe_2O_4$, and $MnFe_2O_4$, calculated by Stoner–Wohlfarth theory, $H_c = 2K/\mu_0 M_s$, are 155 J/m^3, 516 J/m^3, and 92 J/m^3, respectively. K is magneto-crystalline anisotropy constant and μ_0 is vacuum permeability. $CoFe_2O_4$ exhibits higher coercivity, defined by a broadened loop. This is likely due to its higher magneto-crystalline anisotropy in comparison to the other ferrites, which is a result of the spin-orbit contribution[67]. The relationship between H_c and M_s is clearly inversely proportional. This indicates that higher M_s values are associated with lower H_c values[63,68]. Meanwhile, The MNPs have D_m of 6.0–7.2 nm, which is smaller than the particle size in TEM observations. In the end, the quality of magnetic labels in biosensor applications is determined by these magnetic characteristics.

Table 2. Magnetization saturation, remanent, coercivity, magnetic susceptibility, domain size and anisotropy constant of MNPs

Sample	M_s (emu/g)	M_r (emu/g)	H_c (kOe)	χ (.10^{-2})	D_m (nm)	***K*** **(J/m^3)**
Fe_3O_4	55.3	11.6	0.057	4.8	7.2	155
$CoFe_2O_4$	37.6	6.3	0.27	3.5	4.3	516
$MnFe_2O_4$	19.3	1.4	0.097	1.5	6.0	92

3.2 Sensor performance in MNPs assay

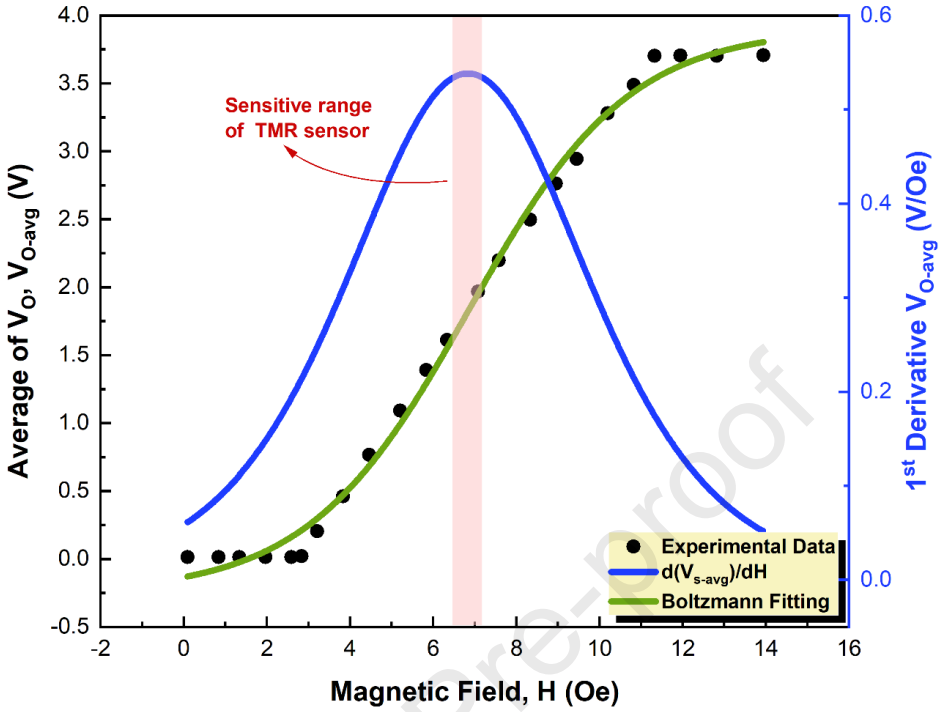

Fig. 8. The magnetic field dependence of output voltage and its derivative for bare TMR sensor.

In the MNPs assay, the TMR-based sensor detects the stray field created by the magnetized MNPs, allowing the determination of their concentration. The stray field of MNP has an intensity of approximately 10^{-2} Oe, whereas the Arduino UNO's effective resolution was at 4.8 mV/unit. Consequently, the minimum sensitivity required for the stray field detection was approximately 480 mV/Oe[52]. According to a datasheet published by NVE, ALT-025 has a sensitivity of approximately 4 mV/Oe[50]. Hence, stray fields cannot be detected owing to their poor sensitivity. The introduction of an amplifier boosts the sensitivity to 437 mV/Oe, thereby meeting the minimal sensitivity criteria. Therefore, the ALT-025 equipped with an amplifier can detect the stray field of the MNPs.

To determine the optimal bias magnetic field for the sensor, the dependence of the output voltage (V_O) on the external magnetic field of a bare-chip TMR sensor was measured within 0–14 Oe. Figure 8 shows that increasing the magnetic field from 3 to 11 Oe led to a rapid and linear increase in the output voltage. The first-order difference of the Boltzmann fitting curve of the output voltage V_O indicates that at H = 6.5–7.2 Oe, the sensor sensitivity reaches its maximum. Therefore, the bias field (H_B) was set at 7 Oe for subsequent detection. Based on the observed low operational magnetic field, it is possible to develop a magnetic field source that is compact, energy efficient, and economically viable.

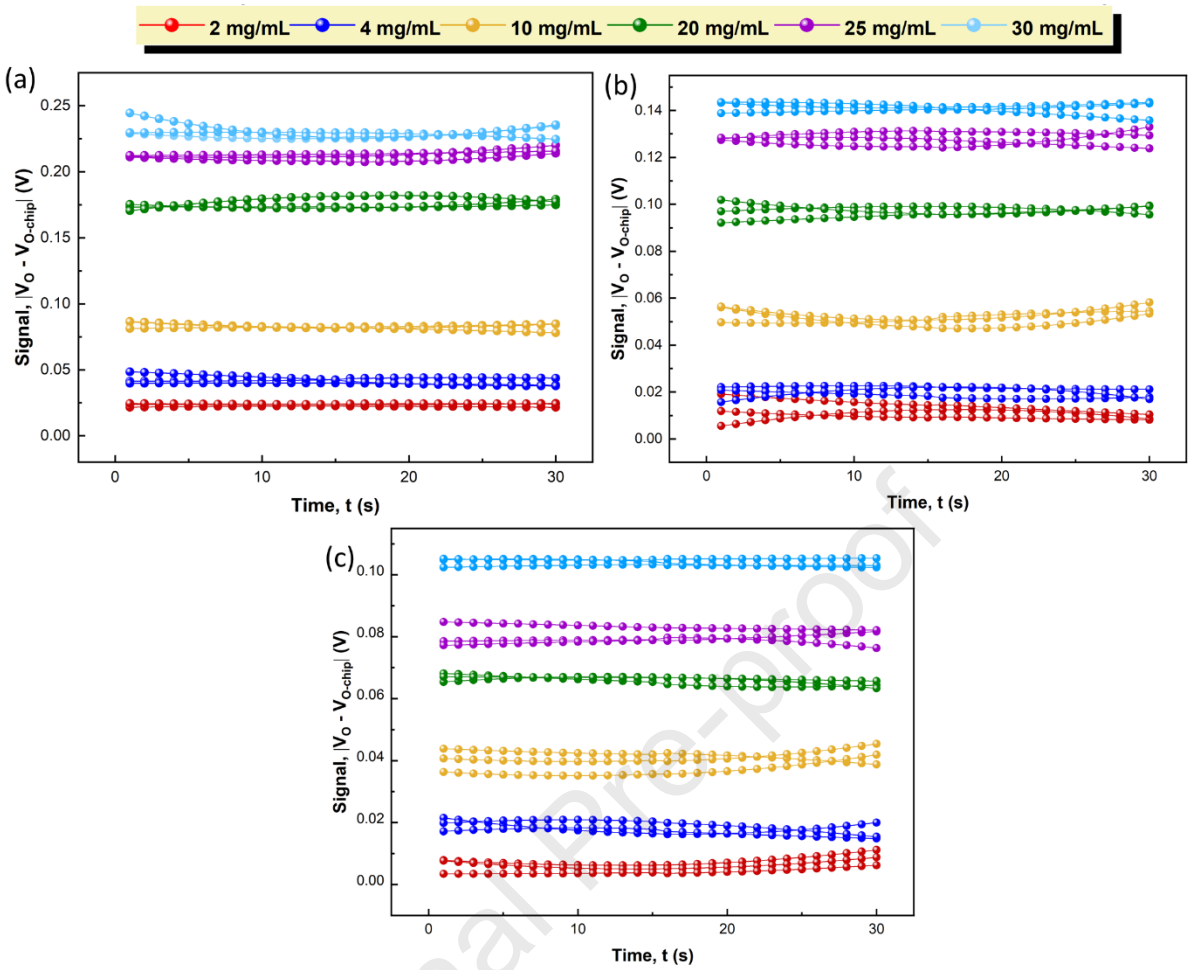

Fig. 9. Repeated measurement of signal for six different concentrations of magnetic labels: (a) Fe_3O_4, (b) $CoFe_2O_4$, and (c) $MnFe_2O_4$.

One of the most important criteria for TMR detection is signal reproducibility. Fig. 8 shows the reproducibility of the sensor when used to detect Fe_3O_4, $CoFe_2O_4$, and $MnFe_2O_4$ at six different concentrations for three repetitions for each type of MNPs. The sensor can differentiate between MNPs concentrations because the signals of each concentration are clustered at the specified value. The repeated testing signal remained steady for 30 s, indicating sensor output stability. Figure 9 shows the relative standard deviations (RSDs) of the sensor signals. When the concentration of the MNPs increased, the relative deviation of the sensor signal decreased exponentially. This declining profile aligns with the characteristic trumpet shape of the Horwitz model. The RSDs for Fe_3O_4, $CoFe_2O_4$, and $MnFe_2O_4$ are 0.8–4.6%; 0.5–22.7%; and 1.0–28.5%, respectively. These results demonstrate that deviations can be reduced by employing MNPs with higher M_S [22]. Relative signal deviations of less than 30% indicate that our sensor has satisfactory reproducibility. In addition, the RSD values for Fe_3O_4 detection were lower than 5%. This value is substantially lower than that achieved in a previous study using a GMR sensor chip, demonstrating the better reproducibility of our sensor[46,52].

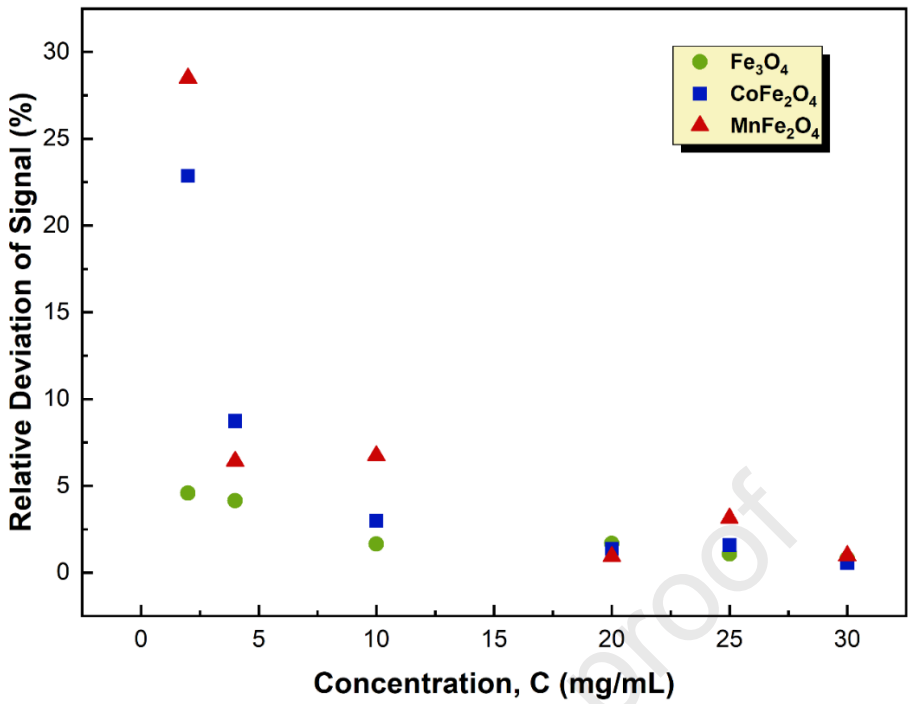

Fig. 10. Relative deviation of the repetition signal measurement.

Figure 11 illustrates the mechanism of the MNPs assay using the TMR sensor. In the absence of H_B exposure, the magnetic moments between the two ferromagnetic layers of the bare-chip TMR were antiparallel. This causes the sensor to have the maximum resistance owing to the low electron tunneling probability between the two ferromagnetic layers, which leads to the lowest output voltage. However, in the presence of H_{Bias}, certain magnetic moments reversed in the same direction as H_{Bias} and increased the probability of electron tunneling. Consequently, the resistivity of the TMR chip was lower than that in the absence of H_{Bias} and the output voltage increased. H_{Bias} functions as a dual-purpose component in this sensor system, changing the magnetization of the free layer and inducing a stray field in the MNPs. In the MNPs assay, an increase in the magnitude of the stray field resulted in a reduction in the effective magnetic field, which affected the TMR sensing element. Therefore, it reduces the number of magnetic moments parallel to the H_{Bias}. Subsequently, the resistivity of the sensor increased and the output voltage decreased. Increased concentrations of MNPs led to a greater number of MNPs being deposited on the surface of the sensor, which subsequently caused a more pronounced stray field and voltage drop.

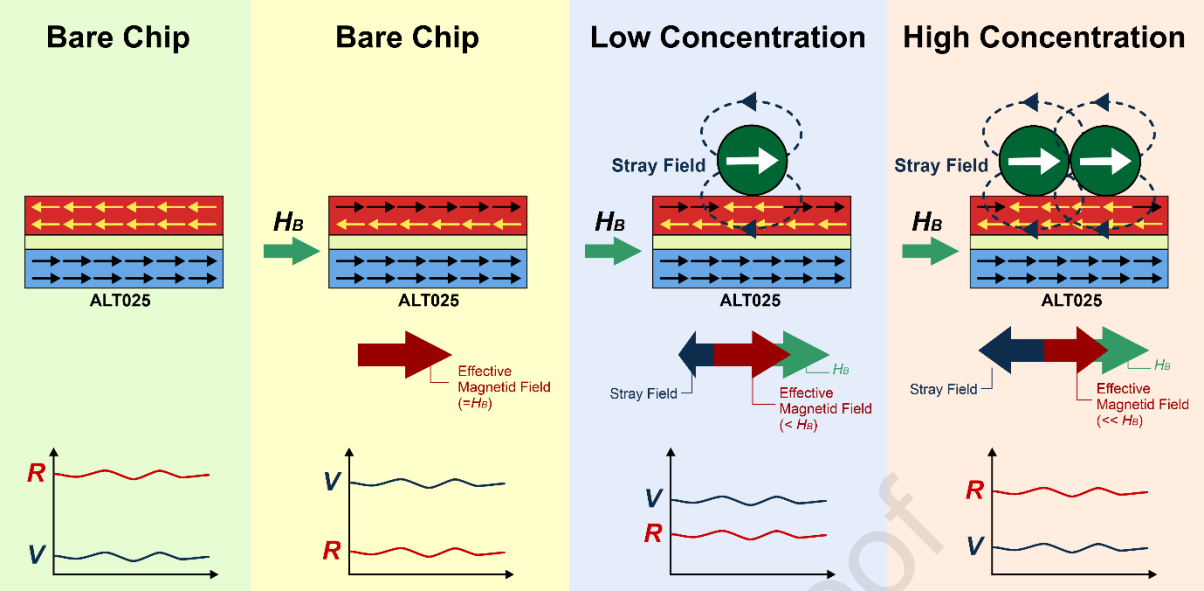

Fig. 11. Illustration of MNP label detection.

Figure 12 depicts the linear dependency of the sensor signal on the FMNP concentration, with a coefficient of determination (R^2) of 0.99 for each of the three MNPs. This excellent linearity demonstrated that the increase in the number of MNPs on the sensor surface was proportional to the stray field. The sensitivity and limit of detection (LOD) that were achieved for the detection of Fe_3O_4 were 7.33 mV/(mg/mL) and 2.11 mg/mL, whereas for that of $CoFe_2O_4$ and $MnFe_2O_4$, sensitivity and LOD were 4.61 mV/(mg/mL), 2.30 mg/mL, and 3.30 mV/(mg/mL), 2.92 mg/mL.

Obviously, Fe_3O_4 exhibit the highest sensitivity with the highest slope, followed by $CoFe_2O_4$ and $MnFe_2O_4$. This is due to Fe_3O_4 generated the strongest stray field at the same concentration owing to its largest M_{Bias}. In contrast, $MnFe_2O_4$ has the lowest M_{Bias}, resulting in the weakest stray field and lowest detection sensitivity. The linear correlation between sensitivity and M_{Bias} for the three MNPs is shown in Fig. 13. The sensitivity of the TMR sensor is directly proportional to M_{Bias}. This implies that particles with a higher M_{Bias} may generate a stronger magnetic dispersion field on the TMR sensor [22]. When M_{Bias} was raised by one Oe, the detection sensitivity increases by 0.34 mV/mg/mL. In summary, a large M_{Bias} enhances the detection signal of TMR biosensors, leading to lower LOD. Because the value of M_{Bias} can vary in direct proportion to the particle size, this outcome validates that the detection signal is directly affected by the particle size. These results also demonstrate that the sensor system can successfully detect MNPs with different stray field intensities.

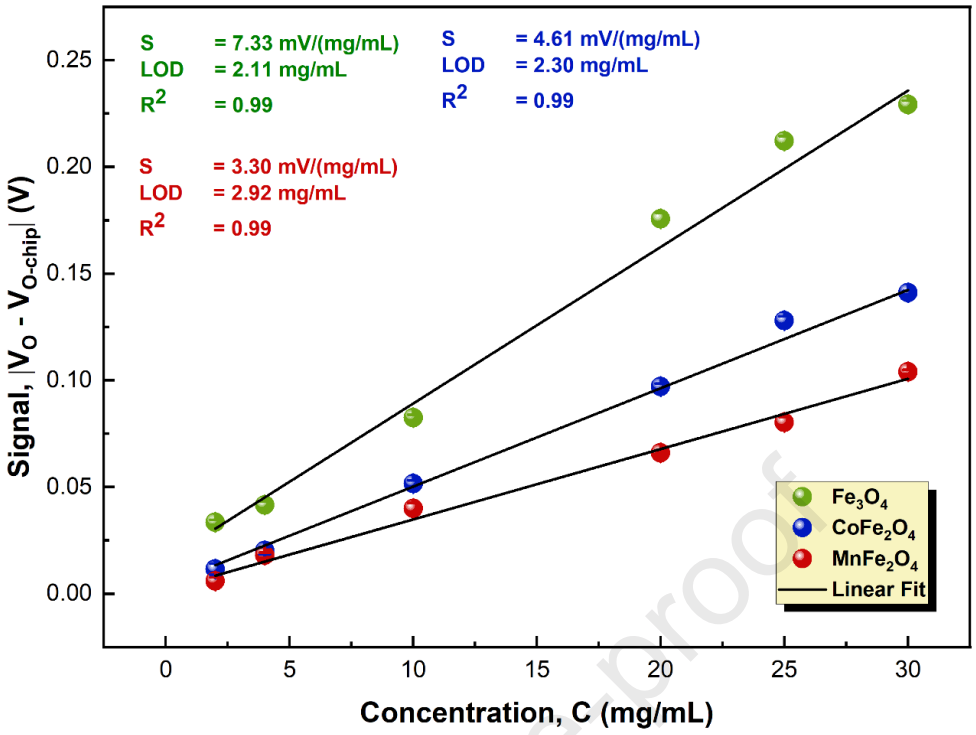

Fig. 12. Dependence of the sensor signal on the concentration of magnetic labels.

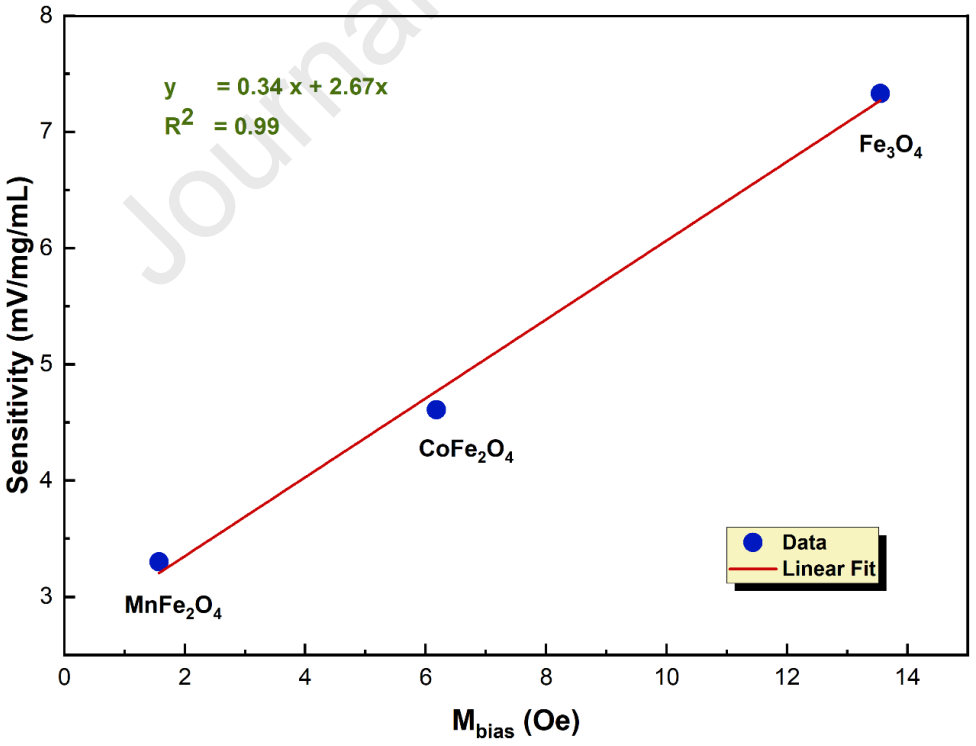

Fig. 13. Magnetization at bias field (M_{Bias}) and detection sensitivity of three particles**.**

No TMR sensor has ever used green-synthesized magnetic nanoparticles as labels. However, in our previous study, Fe_3O_4 MNPs synthesized using the same green synthesis method (GS-Fe_3O_4) were used as labels for detection using a GMR sensor. In addition, the detection performance was compared using Fe_3O_4 nanoparticles synthesized by standard methods (SM-Fe_3O_4). In prior studies, the VSM test results showed that the magnetization value of GS-Fe_3O_4 is competitive as a magnetic label[46]. Figure 14 compares the detection results of GS-Fe_3O_4 using the TMR sensor (this study) and those of GS-Fe_3O_4 and SM-Fe_3O_4 using the GMR sensor. The sensitivity of detecting GS-Fe_3O_4 with the TMR sensor was higher than that with the GMR sensor for both GS-Fe_3O_4 and SM-Fe_3O_4. These results demonstrate that the TMR sensor is capable of accurately detecting variations in stray fields caused by changes in the concentration of GS-Fe_3O_4. Therefore, it can be concluded that the GS-ferrite is comparable to those fabricated using popular standard methods.

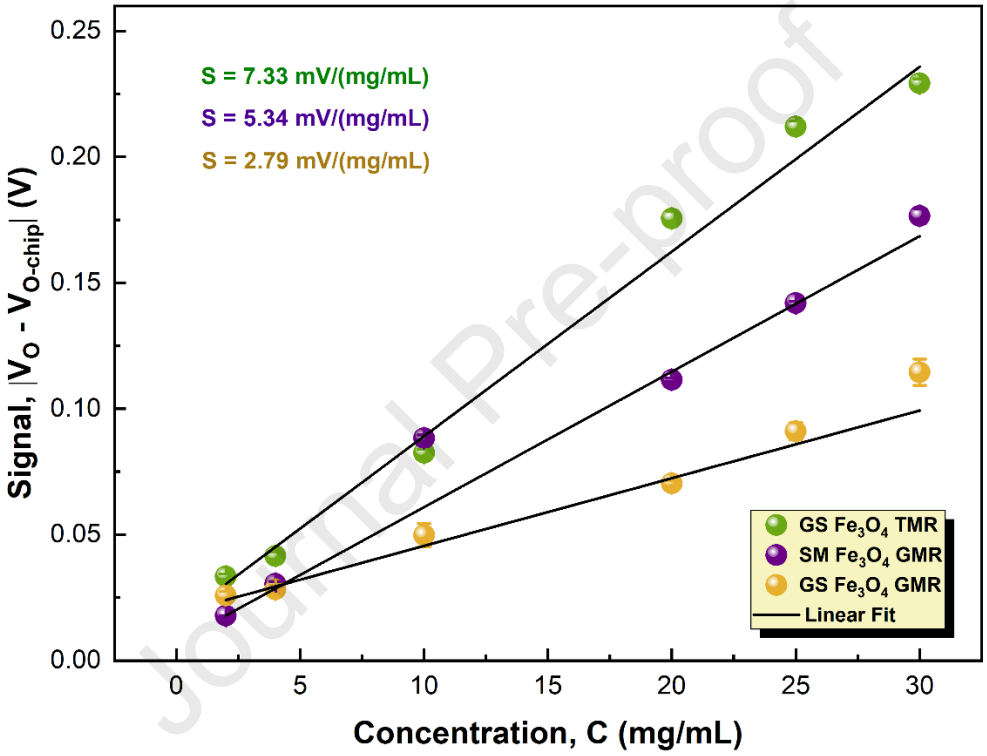

Fig. 14. TMR and GMR sensors' performances to detect GS-Fe_3O_4 and SM-Fe_3O_4 [46]

The performance of our sensor system compared with that of the most recent MR sensor based on MR in detecting MNPs is presented in Table 4. Our sensor outperforms the others by producing a higher output voltage with a simple measurement setup, eliminating the need for a costly additional voltage gauge. Moreover, our sensor's sensitivity is quite promising, and it has been shown that it can detect MNPs with lower M_s. Compared with detection using GMR NVE AAL-024, our sensor exhibits higher sensitivity, even for the detection of MNPs with lower M_s. Furthermore, it also shows higher sensitivity compared to the detection of commercial labels. This further indicates that GS ferrites can be considered potential alternative labels.

Table 4. Performance comparison of MR-based sensor in detecting MNPs.

Sensors	Samples	Particle Size (nm)	M_s [emu/g]	Sensitivity (mV/(mg/mL))	Output voltage (mV)
GMR Chip GF708 **[21]**	$MnFe_2O_4$	685	62.0	11.84	0.04–3
GMR Chip GF708 **[23]**	Fe_3O_4	80–580	62.2–74.2	495.00	2.14–2.24
GMR Chip NVE AAL-024 [46]	Fe_3O_4 GS-Fe_3O_4	14 11	77.7 55.0	7.33 2.79	10–220 7–160
TMR Chip by Tsinghua Univ. [3]	Commercial Fe_3O_4/Carboxyl	-	-	-	2–35
TMR chip by Multi dimension [69]	Commercial Superparamagnetic Bead	2800	-	3.00	5–40
TMR Chip NVE-ALT025 (This work)	GS-Fe_3O_4 GS-$CoFe_2O_4$ GS-$MnFe_2O_4$	10.3 9.2 6.1	55.3 37.6 19.3	7.33 4.61 3.30	23.4–263.3 11.5–166.8 5.9–156.6

4. Conclusion

A simple and low-cost commercial chip-based TMR sensor was developed for a green MNPs assay. The sensor exhibited good performance in detecting three types of ferrite-based MNPs. The sensor provides a real-time, stable, and reproducible signal for 30 s, demonstrating its ability to facilitate the rapid detection of MNPs. Moreover, the sensor exhibited an excellent linear response to the concentration of MNPs (R^2=0.99) with a low LOD. Even for ferrite-based MNPs with a low saturation magnetization, variations in the output voltage can be readily detected by the sensor via the disparity in the stray field intensity produced by the three types of MNPs. The particle size affects magnetization, thereby influencing the output voltage of the sensor. Because the sensitivity of detection is directly proportional to the bias magnetization, particles possessing higher bias magnetization can produce a stronger magnetic stray field on the TMR sensor. The sensor system effectively identified MNPs with varying stray field intensities. Based on these results, the coupling of commercial chip-based TMR sensors and green-synthesized MNPs has significant potential for the rapid, responsive, and easy-to-use detection of various targeted biomolecules.

Funding

This work was supported by Center for Education Financial Services (Puslapdik), Indonesia Endowment Funds for Education (LPDP), and Ministry of Education, Culture, Research, and Technology, Republic of Indonesia.

Acknowledgments

The authors would like to thank Prof. Takeshi Kato (Institute of Materials and Systems for Sustainability, Nagoya University, Nagoya, Japan) and Dr. Daiki Oshima (Department of Electronics, Nagoya University, Nagoya, Japan) for facility access in their laboratory for using vibrating sample magnetometer (VSM, Riken Denshi Co., Ltd.).

Declaration of Competing Interest

The authors declare that they have no known competing financial interests or personal relationships that could have appeared to influence the work reported in this paper.

References

[1] H. Lei, K. Wang, X. Ji, D. Cui, Contactless measurement of magnetic nanoparticles on lateral flow strips using tunneling magnetoresistance (TMR) sensors in differential configuration, Sensors (Switzerland) 16 (2016). https://doi.org/10.3390/s16122130.

[2] X. Wang, Y. Luo, K. Huang, N. Cheng, Biosensor for agriculture and food safety: Recent advances and future perspectives, Advanced Agrochem 1 (2022) 3–6. https://doi.org/10.1016/j.aac.2022.08.002.

[3] X.H. Mu, H.F. Liu, Z.Y. Tong, B. Du, S. Liu, B. Liu, Z.W. Liu, C. Gao, J. Wang, H. Dong, A new rapid detection method for ricin based on tunneling magnetoresistance biosensor, Sens Actuators B Chem 284 (2019) 638–649. https://doi.org/10.1016/j.snb.2018.12.127.

[4] P.P. Sharma, E. Albisetti, M. Massetti, M. Scolari, C. La Torre, M. Monticelli, M. Leone, F. Damin, G. Gervasoni, G. Ferrari, F. Salice, E. Cerquaglia, G. Falduti, M. Cretich, E. Marchisio, M. Chiari, M. Sampietro, D. Petti, R. Bertacco, Integrated platform for detecting pathogenic DNA via magnetic tunneling junction-based biosensors, Sens Actuators B Chem 242 (2017) 280–287. https://doi.org/10.1016/j.snb.2016.11.051.

[5] S. Liang, P. Sutham, K. Wu, K. Mallikarjunan, J.P. Wang, Giant Magnetoresistance Biosensors for Food Safety Applications, Sensors 22 (2022). https://doi.org/10.3390/s22155663.

[6] C. Ren, Q. Bayin, S. Feng, Y. Fu, X. Ma, J. Guo, Biomarkers detection with magnetoresistance-based sensors, Biosens Bioelectron 165 (2020). https://doi.org/10.1016/j.bios.2020.112340.

[7] I. Giouroudi, E. Hristoforou, Perspective: Magnetoresistive sensors for biomedicine, J Appl Phys 124 (2018). https://doi.org/10.1063/1.5027035.

[8] H.T. Huang, P. Garu, C.H. Li, W.C. Chang, B.W. Chen, S.Y. Sung, C.M. Lee, J.Y. Chen, T.F. Hsieh, W.J. Sheu, H. Ouyang, W.C. Wang, C.R. Chang, C.L. Wang, M.S. Hsu, Z.H. Wei, Magnetoresistive Biosensors for Direct Detection of Magnetic Nanoparticle Conjugated Biomarkers on a Chip, SPIN 9 (2019). https://doi.org/10.1142/S2010324719400022.

[9] D. Su, K. Wu, R. Saha, C. Peng, J.P. Wang, Advances in magnetoresistive biosensors, Micromachines (Basel) 11 (2020). https://doi.org/10.3390/mi11010034.

[10] E.M. Materón, C.M. Miyazaki, O. Carr, N. Joshi, P.H.S. Picciani, C.J. Dalmaschio, F. Davis, F.M. Shimizu, Magnetic nanoparticles in biomedical applications: A review, Applied Surface Science Advances 6 (2021). https://doi.org/10.1016/j.apsadv.2021.100163.

[11] M. Virumbrales, V. Blanco-Gutiérrez, A. Delgado-Cabello, R. Sáez-Puche, M.J. Torralvo, Superparamagnetism in CoFe2O4 nanoparticles: An example of a collective magnetic behavior dependent on the medium, J Alloys Compd 767 (2018) 559–566. https://doi.org/10.1016/j.jallcom.2018.07.096.

[12] B. Cao, K. Wang, H. Xu, Q. Qin, J. Yang, W. Zheng, Q. Jin, D. Cui, Development of magnetic sensor technologies for point-of-care testing: Fundamentals, methodologies and applications, Sens Actuators A Phys 312 (2020) 112130. https://doi.org/10.1016/j.sna.2020.112130.

[13] W. Su, Z. Wang, T. Wen, Z. Hu, J. Wu, Z. Zhou, M. Liu, Linear Anisotropic Magnetoresistive Sensor Without Barber-Pole Electrodes, IEEE Electron Device Letters 40 (2019) 969–972. https://doi.org/10.1109/LED.2019.2913506.

[14] Z. Wang, T. Wen, W. Su, C. Hu, Y. Chen, Z. Hu, J. Wu, Z. Zhou, M. Liu, Magnetic Sensor Based on Giant Magneto-Impedance in Commercial Inductors, IEEE Transactions on Industrial Electronics 68 (2021) 7577–7583. https://doi.org/10.1109/TIE.2020.3007097.

[15] Z. Jin, T.M. Koo, M.S. Kim, M. Al-Mahdawi, M. Oogane, Y. Ando, Y.K. Kim, Highly-sensitive magnetic sensor for detecting magnetic nanoparticles based on magnetic tunnel junctions at a low static field, AIP Adv 11 (2021). https://doi.org/10.1063/9.0000189.

[16] M.A. Khan, J. Sun, B. Li, A. Przybysz, J. Kosel, Magnetic sensors-A review and recent technologies, Engineering Research Express 3 (2021). https://doi.org/10.1088/2631-8695/ac0838.

[17] N.A. Wibowo, C. Kurniawan, D.K.A. Kusumahastuti, A. Setiawan, E. Suharyadi, Review—Potential of Tunneling Magnetoresistance Coupled to Iron Oxide Nanoparticles as a Novel Transducer for Biosensors-on-Chip, J Electrochem Soc 171 (2024) 017512. https://doi.org/10.1149/1945-7111/ad1f35.

[18] M.K. Shobana, Nanoferrites in biosensors – A review, Mater Sci Eng B Solid State Mater Adv Technol 272 (2021). https://doi.org/10.1016/j.mseb.2021.115344.

[19] C.R. Kalaiselvan, S.S. Laha, S.B. Somvanshi, T.A. Tabish, N.D. Thorat, N.K. Sahu, Manganese ferrite (MnFe2O4) nanostructures for cancer theranostics, Coord Chem Rev 473 (2022). https://doi.org/10.1016/j.ccr.2022.214809.

[20] A. Tripathy, M.J. Nine, F.S. Silva, Biosensing platform on ferrite magnetic nanoparticles: Synthesis, functionalization, mechanism and applications, Adv Colloid Interface Sci 290 (2021). https://doi.org/10.1016/j.cis.2021.102380.

[21] J. Xu, Q. Li, X.Y. Gao, F.F. Leng, M. Lu, P.Z. Guo, G.X. Zhao, S.D. Li, Detection of the Concentration of MnFe2O4 Magnetic Microparticles Using Giant Magnetoresistance Sensors, IEEE Trans Magn 52 (2016). https://doi.org/10.1109/TMAG.2015.2497249.

[22] Y. Zhang, J. Xu, D. Cao, Q. Li, G. Zhao, N.X. Sun, S. Li, The influence of bias magnetization of nanoparticles on GMR sensor signal and sensitivity for the ultra-low concentration detection, J Magn Magn Mater 453 (2018) 132–136. https://doi.org/10.1016/j.jmmm.2018.01.010.

[23] Y. Zhang, J. Xu, Q. Li, D. Cao, S. Li, The effect of the particle size and magnetic moment of the Fe 3 O 4 superparamagnetic beads on the sensitivity of biodetection, AIP Adv 9 (2019). https://doi.org/10.1063/1.5050034.

[24] P.E. Swastika, G. Antarnusa, E. Suharyadi, T. Kato, S. Iwata, Biomolecule detection using wheatstone bridge giant magnetoresistance (GMR) sensors based on CoFeB spin-valve thin film, in: J Phys Conf Ser, IOP Publishing, 2018: p. 12060.

[25] G. Antarnusa, P.E. Swastika, E. Suharyadi, Wheatstone bridge-giant magnetoresistance (GMR) sensors based on Co/Cu multilayers for bio-detection applications, in: J Phys Conf Ser, IOP Publishing, 2018: p. 12061.

[26] E. Suharyadi, T. Alfansuri, L.S. Handriani, N.A. Wibowo, H. Sabarman, Detection of Fe3O4/PEG nanoparticles using one and two spin-valve GMR sensing elements in wheatstone bridge circuit, Journal of Materials Science: Materials in Electronics 32 (2021) 23958–23967. https://doi.org/10.1007/s10854-021-06859-6.

[27] E. Suharyadi, I. Pardede, F.A. Hasibuan, Giant Magnetoresistance (GMR) Sensors Based on Co/Cu Multilayers for Biomaterial Detection Applications, 2016.

[28] I. Nurpriyanti, I. Pardede, E. Suharyadi, Detection of Fe3O4 Magnetic Nanoparticles using Giant Magnetoresistance (GMR) Sensor Based on Multilayer and Spin Valve

Thin Films by Wheatstone Bridge Circuit, in: 2016 International Seminar on Sensors, Instrumentation, Measurement and Metrology (ISSIMM), IEEE, Malang, 2016: pp. 32–36.

[29] K.L. Routray, S. Saha, D. Behera, Green synthesis approach for nano sized CoFe2O4 through aloe vera mediated sol-gel auto combustion method for high frequency devices, Mater Chem Phys 224 (2019) 29–35. https://doi.org/10.1016/j.matchemphys.2018.11.073.

[30] Y.P. Yew, K. Shameli, M. Miyake, N.B.B. Ahmad Khairudin, S.E.B. Mohamad, T. Naiki, K.X. Lee, Green biosynthesis of superparamagnetic magnetite Fe3O4 nanoparticles and biomedical applications in targeted anticancer drug delivery system: A review, Arabian Journal of Chemistry 13 (2020) 2287–2308. https://doi.org/10.1016/j.arabjc.2018.04.013.

[31] M. Khatami, H.Q. Alijani, M.S. Nejad, R.S. Varma, Core@ shell nanoparticles: greener synthesis using natural plant products, Applied Sciences 8 (2018) 411.

[32] E.C. Nnadozie, P.A. Ajibade, Green synthesis and characterization of magnetite (Fe3O4) nanoparticles using Chromolaena odorata root extract for smart nanocomposite, Mater Lett 263 (2020). https://doi.org/10.1016/j.matlet.2019.127145.

[33] A. Kiani, F. Davar, M. Bazarganipour, Influence of verjuice extract on the morphology, phase, and magnetic properties of green synthesized CoFe2O4 nanoparticle: its application as an anticancer drug delivery, Ceram Int 48 (2022) 34895–34906. https://doi.org/10.1016/j.ceramint.2022.08.079.

[34] A. Mohammadpour, N. Karami, R. Zabihi, E. Fazeliyan, A. Abbasi, S. Karimi, M. Barbosa de Farias, M.G. Adeodato Vieira, E. Shahsavani, A. Mousavi Khaneghah, Green synthesis, characterization, and application of Fe3O4 nanoparticles for methylene blue removal: RSM optimization, kinetic, isothermal studies, and molecular simulation, Environ Res 225 (2023). https://doi.org/10.1016/j.envres.2023.115507.

[35] L. Katata-Seru, T. Moremedi, O.S. Aremu, I. Bahadur, Green synthesis of iron nanoparticles using Moringa oleifera extracts and their applications: Removal of nitrate from water and antibacterial activity against Escherichia coli, J Mol Liq 256 (2018) 296–304. https://doi.org/10.1016/j.molliq.2017.11.093.

[36] N. Madubuonu, S.O. Aisida, A. Ali, I. Ahmad, T. kai Zhao, S. Botha, M. Maaza, F.I. Ezema, Biosynthesis of iron oxide nanoparticles via a composite of Psidium guavaja-Moringa oleifera and their antibacterial and photocatalytic study, J Photochem Photobiol B 199 (2019). https://doi.org/10.1016/j.jphotobiol.2019.111601.

[37] S.S. Banifatemi, F. Davar, B. Aghabarari, J.A. Segura, F.J. Alonso, S.M. Ghoreishi, Green synthesis of CoFe2O4 nanoparticles using olive leaf extract and characterization of their magnetic properties, Ceram Int 47 (2021) 19198–19204. https://doi.org/10.1016/j.ceramint.2021.03.267.

[38] F. Golrizkhatami, L. Taghavi, N. Nasseh, H.A. Panahi, Synthesis of novel MnFe2O4/BiOI green nanocomposite and its application to photocatalytic degradation of tetracycline hydrochloride: (LC-MS analyses, mechanism, reusability, kinetic, radical agents, mineralization, process capability, and purification of actual pharmaceutical wastewater), J Photochem Photobiol A Chem 444 (2023). https://doi.org/10.1016/j.jphotochem.2023.114989.

[39] A. V. Ramesh, D. Rama Devi, S. Mohan Botsa, K. Basavaiah, Facile green synthesis of Fe 3 O 4 nanoparticles using aqueous leaf extract of Zanthoxylum armatum DC. for efficient adsorption of methylene blue, Journal of Asian Ceramic Societies 6 (2018) 145–155. https://doi.org/10.1080/21870764.2018.1459335.

[40] H. Şengönül, O. Demircan, Synthesis and Characterization of Fe3O4 Nanoparticles Using Prunus serrulata Leaf Extract, Bionanoscience 13 (2023) 1944–1954. https://doi.org/10.1007/s12668-023-01174-2.

[41] C. Silveira, Q.L. Shimabuku, M. Fernandes Silva, R. Bergamasco, Iron-oxide nanoparticles by the green synthesis method using Moringa oleifera leaf extract for fluoride removal, Environmental Technology (United Kingdom) 39 (2018) 2926–2936. https://doi.org/10.1080/09593330.2017.1369582.

[42] P.K. Gautam, S. Shivalkar, S. Banerjee, Synthesis of M. oleifera leaf extract capped magnetic nanoparticles for effective lead [Pb (II)] removal from solution: Kinetics, isotherm and reusability study, J Mol Liq 305 (2020). https://doi.org/10.1016/j.molliq.2020.112811.

[43] R.K. Saini, I. Sivanesan, Y.S. Keum, Phytochemicals of Moringa oleifera: a review of their nutritional, therapeutic and industrial significance, 3 Biotech 6 (2016). https://doi.org/10.1007/s13205-016-0526-3.

[44] N.Z.A. Rani, K. Husain, E. Kumolosasi, Moringa genus: A review of phytochemistry and pharmacology, Front Pharmacol 9 (2018). https://doi.org/10.3389/fphar.2018.00108.

[45] N. Mabarroh, T. Alfansuri, N. Aji Wibowo, N. Imani Istiqomah, R. Marsel Tumbelaka, E. Suharyadi, Detection of green-synthesized magnetite nanoparticles using spin-valve GMR-based sensor and their potential as magnetic labels, J Magn Magn Mater 560 (2022). https://doi.org/10.1016/j.jmmm.2022.169645.

[46] H. Ardiyanti, N. Mabarroh, N.A. Wibowo, N.I. Istiqomah, R.M. Tumbelaka, M.A. Ulil Absor, E. Suharyadi, New design of a commercial chip-based GMR sensor with magnetite nanoparticles for biosensing applications, Journal of Science: Advanced Materials and Devices 8 (2023). https://doi.org/10.1016/j.jsamd.2023.100556.

[47] S. Garcia, N. Mabarroh, M.Y. Darmawan, N.A. Wibowo, H. Ardiyanti, R.M. Tumbelaka, N.I. Istiqomah, E. Suharyadi, Two spin-valve GMR thin films on half wheatstone bridge circuit for detecting green-synthesized Fe3O4@Ag nanoparticles-labeled biomolecule, Materialia (Oxf) 32 (2023). https://doi.org/10.1016/j.mtla.2023.101930.

[48] S. Yan, Z. Zhou, Y. Yang, Q. Leng, W. Zhao, Developments and Applications of Tunneling Magnetoresistance Sensors, 2022. http://creativecommons.org/licenses/by/4.0/.

[49] D.R. Mũoz, J.S. Moreno, S.C. Berga, E.C. Montero, C.R. Escrìv, A.E.N. Antón, Temperature compensation of Wheatstone bridge magnetoresistive sensors based on generalized impedance converter with input reference current, in: Review of Scientific Instruments, 2006. https://doi.org/10.1063/1.2358696.

[50] TMR Analog Sensors ALT02x TMR Analog Magnetometer Sensors, n.d. www.nve.com.

[51] W. Gao, X. Luo, Y. Liu, Y. Zhao, Y. Cui, Development of an arduino-based integrated system for sensing of hydrogen peroxide, Sensors and Actuators Reports 3 (2021). https://doi.org/10.1016/j.snr.2021.100045.

[52] N.A. Wibowo, H. Sabarman, E. Suharyadi, A New Platform of Iron Oxide-Based Nanoparticles Assay Using GMR Chip-Based Sensor With Microcontroller, IEEE Sens J 22 (2022) 20093–20101. https://doi.org/10.1109/JSEN.2022.3207213.

[53] D. Acharya, A. Rani, S. Agarwal, V. Singh, Application of adaptive Savitzky–Golay filter for EEG signal processing, Perspect Sci (Neth) 8 (2016) 677–679. https://doi.org/10.1016/j.pisc.2016.06.056.

[54] H.F. Kiwumulo, H. Muwonge, C. Ibingira, M. Lubwama, J.B. Kirabira, R.T. Ssekitoleko, Green synthesis and characterization of iron-oxide nanoparticles using

Moringa oleifera: a potential protocol for use in low and middle income countries, BMC Res Notes 15 (2022). https://doi.org/10.1186/s13104-022-06039-7.

[55] G.C. Hermosa, C.S. Liao, H.S. Wu, S.F. Wang, T.Y. Liu, K.S. Jeng, S.S. Lin, C.F. Chang, A.C.A. Sun, Green Synthesis of Magnetic Ferrites (Fe3O4, CoFe2O4, and NiFe2O4) Stabilized by Aloe Vera Extract for Cancer Hyperthermia Activities, IEEE Trans Magn 58 (2022). https://doi.org/10.1109/TMAG.2022.3158835.

[56] N.A. Wibowo, J. Juharni, H. Sabarman, E. Suharyadi, A Spin-Valve GMR Based Sensor with Magnetite@silver Core-Shell Nanoparticles as a Tag for Bovine Serum Albumin Detection, ECS Journal of Solid State Science and Technology 10 (2021) 107002. https://doi.org/10.1149/2162-8777/ac2d4e.

[57] M. Jafari Eskandari, I. Hasanzadeh, Size-controlled synthesis of Fe3O4 magnetic nanoparticles via an alternating magnetic field and ultrasonic-assisted chemical co-precipitation, Materials Science and Engineering: B 266 (2021). https://doi.org/10.1016/j.mseb.2021.115050.

[58] L.H. Nguyen, N.H. Nam, L.T. Tam, D. Van Tuan, N.X. Truong, N. Van Quynh, P. Thi Hong Tuyet, H.P. Thu, D.H. Manh, P.T. Phong, P.H. Nam, Effect of Gd substitution on structure, optical and magnetic properties, and heating efficiency of Fe3O4 nanoparticles for magnetic hyperthermia applications, J Alloys Compd 968 (2023). https://doi.org/10.1016/j.jallcom.2023.172205.

[59] V.T. Sivanandan, A.S. Prasad, Impact of Green Synthesis on Crystallographic Structure, Optical and Magnetic Properties of Nanocrystalline CoFe2O4, J Electron Mater (2023). https://doi.org/10.1007/s11664-023-10354-5.

[60] P. Iranmanesh, S. Saeednia, M. Mehran, S.R. Dafeh, Modified structural and magnetic properties of nanocrystalline MnFe2O4 by pH in capping agent free co-precipitation method, J Magn Magn Mater 425 (2017) 31–36. https://doi.org/10.1016/j.jmmm.2016.10.105.

[61] C. Murugesan, K. Ugendar, L. Okrasa, J. Shen, G. Chandrasekaran, Zinc substitution effect on the structural, spectroscopic and electrical properties of nanocrystalline MnFe2O4 spinel ferrite, Ceram Int 47 (2021) 1672–1685. https://doi.org/10.1016/j.ceramint.2020.08.284.

[62] P. Kumar, S. Pathak, K. Jain, A. Singh, Kuldeep, G.A. Basheed, R.P. Pant, Low-temperature large-scale hydrothermal synthesis of optically active PEG-200 capped single domain MnFe2O4 nanoparticles, J Alloys Compd 904 (2022). https://doi.org/10.1016/j.jallcom.2022.163992.

[63] R.B. Kamble, V. Varade, K.P. Ramesh, V. Prasad, Domain size correlated magnetic properties and electrical impedance of size dependent nickel ferrite nanoparticles, AIP Adv 5 (2015). https://doi.org/10.1063/1.4906101.

[64] Z. Ma, J. Mohapatra, K. Wei, J.P. Liu, S. Sun, Magnetic Nanoparticles: Synthesis, Anisotropy, and Applications, Chem Rev 123 (2023) 3904–3943. https://doi.org/10.1021/acs.chemrev.1c00860.

[65] W.N. Jannah, A. Taufiq, S. Zulaikah, A. Hidayat, E. Suharyadi, S.T. Wicaksono, S. Sunaryono, Fe3O4–graphene/polyethylene glycol–SiO2 as a phase change material for thermal energy storage, Mater Chem Phys 310 (2023). https://doi.org/10.1016/j.matchemphys.2023.128457.

[66] V.H. Ojha, K.M. Kant, Temperature dependent magnetic properties of superparamagnetic CoFe2O4 nanoparticles, Physica B Condens Matter 567 (2019) 87–94. https://doi.org/10.1016/j.physb.2019.04.035.

[67] N. Bao, L. Shen, Y. Wang, P. Padhan, A. Gupta, A facile thermolysis route to monodisperse ferrite nanocrystals, J Am Chem Soc 129 (2007) 12374–12375. https://doi.org/10.1021/ja074458d.

[68] J.N. Dahal, D. Neupane, T.P. Poudel, Synthesis and magnetic properties of 4:1 hard-soft SrFe12O19-La1-xSrxMnO3 nanocomposite prepared by auto-combustion method, AIP Adv 9 (2019). https://doi.org/10.1063/1.5096530.

[69] Y. Wu, Y. Liu, Q. Zhan, J.P. Liu, R.W. Li, Rapid detection of Escherichia coli O157:H7 using tunneling magnetoresistance biosensor, AIP Adv 7 (2017). https://doi.org/10.1063/1.4977017.

Highlights: Journal

- Fe_3O_4, $CoFe_2O_4$ and $MnFe_2O_4$ were synthesized by the green route by coprecipitation method using *Moringa oleifera* extract.
- The TMR sensor shows high sensitivity and low limit of detection in detecting green-synthesized MNPs.
- The sensitivity of MNPs detection is directly proportional to their bias magnetization.
- The TMR sensor system can detect various stray field strengths of MNPs, even for MNPs with low saturation magnetization.

Declaration of Competing Interest

The authors declare that they have no known competing financial interests or personal relationships that could have appeared to influence the work reported in this paper.